Electronic, magnetic, and structural properties of NiFeMnAl

Pavel V. Lukashev, ¹ Jax Wysong², Stephen McFadden, ¹ Gavin Baker², Brandon Schmidt, ¹ Paul M. Shand, ¹ Parashu Kharel²

¹Department of Physics, University of Northern Iowa, Cedar Falls, IA 50614, USA ²Department of Chemistry, Biochemistry, and Physics, South Dakota State University, Brookings, SD 57007, USA

Abstract

Half-metallic Heusler compounds have been extensively studied in the recent years, both experimentally and theoretically, for potential applications in spin-based electronics. Here, we present the results of a combined theoretical and experimental study of the quaternary Heusler compound NiFeMnAl. Our calculations indicate that this material is half-metallic in the ground state and maintains its half-metallic electronic structure under a considerable range of external hydrostatic pressure and biaxial strain. NiFeMnAl crystallizes in the regular cubic Heusler structure, and exhibits ferromagnetic alignment. The practical feasibility of the proposed system is confirmed in the experimental section of this work. More specifically, a bulk ingot of NiFeMnAl was synthesized in A2 type disordered cubic structure using arc melting. It shows a high Curie temperature of about 468 K and a saturation magnetization of 2.3 $\mu_B/f.u$. The measured magnetization value is smaller than the one calculated for the ordered structure. This discrepancy is likely due to the A2 type atomic disorder, as demonstrated by our calculations. We hope that the presented results may be useful for researchers working on practical applications of spin-based electronics.

I. Introduction

The existence of half-metallic materials was predicted in 1983 by de Groot et al. As their name suggests, these compounds are conducting for electrons of one spin, and insulating (semiconducting) for the electrons of the opposite spin. This makes their spin polarization, P equal to 100%, where P is defined as $P = \frac{N_{\uparrow}(\epsilon_F) - N_{\downarrow}(\epsilon_F)}{N_{\uparrow}(\epsilon_F) + N_{\downarrow}(\epsilon_F)}$, with $N_{\uparrow,\downarrow}(\epsilon_F)$ being the spin-dependent density of states (DOS) at the Fermi level, ϵ_F . As such, half-metallic systems are ideal candidates for applications in spin-transport electronics (spintronics), where highly spin-polarized currents are desired. At the same time, various physical mechanisms may reduce the spin polarization of these

compounds. For example, it has been reported that the surfaces and / or interfaces of these materials are typically not half-metallic, ^{3,4,5,6,7,8,9} although in certain cases half-metallicity may be restored by interface engineering. ^{10,11}

Among various materials considered for practical applications in spintronics, Heusler alloys have attracted particular attention in recent years, largely due to their high Curie temperature, often significantly higher than the room temperature. ^{12, 13, 14, 15, 16, 17, 18} Many Heusler compounds have been theoretically predicted to be half-metallic, ^{19, 20} and in some cases the half-metallicity was confirmed experimentally. ^{21, 22, 23, 24} In addition to half-metallicity, Heusler alloys have been also reported to exhibit other interesting properties, such as shape-memory effects ^{25, 26} and topological states. ^{27, 28} The combination of these multifunctional properties makes Heusler materials one of the prime candidates for practical applications in modern spintronic devices.

In this work, we perform a combined theoretical and experimental study of NiFeMnAl, a quaternary Heusler compound that has been recently reported by Gao, Opahle, and Zhang to be spin-gapless semiconducting (SGS). Spin-gapless semiconductors represent a new class of materials, the existence of which was predicted by Wang. These materials are semiconducting for electrons of one spin, while for the opposite spin they have a gapless electronic structure. In SGS materials, both electrons and holes are 100% spin-polarized. Spin-gapless semiconductivity has been reported in various systems, including oxides and Heusler alloys. Here we show that while the electronic structure of NiFeMnAl indeed has SGS-like characteristics, this material is half-metallic in its ground state. At the same time, it may undergo a transition to an SGS state under negative pressure (expansion), which may, at least in principle, be achieved by atomic substitution. The practical feasibility and thermodynamic stability of the considered compound is confirmed by synthesizing bulk samples of NiFeMnAl, as discussed in the experimental section of this work.

The rest of this paper is organized as follows. In Section II, we outline the computational methods and experimental techniques. In Section III, we present our main results, both computational (sub-section III-a) and experimental (sub-section III-b). Section IV contains conclusions, and it is followed by acknowledgments and references to the representative relevant publications.

II. Methods

II. a) Computational methods

We performed density functional calculations, as implemented in the Vienna *ab initio* simulation package (VASP). ³⁵ In particular, we used the projector augmented-wave method (PAW). ³⁶ and generalized-gradient approximation (GGA) method suggested by Perdew, Burke, and Ernzerhof. ³⁷ In addition, the integration method by Methfessel and Paxton with a 5×10^{-2} eV width of smearing is used. ³⁸ The energy convergence criterion of 10^{-3} meV is used for electronic and magnetic structure calculations, while the geometry optimizations are performed with a less strict criterion of 10^{-2} meV. The structural optimizations are performed with a *k*-point mesh of $4\times4\times4$, while a *k*-mesh of $12\times12\times12$ is used for electronic structure calculations. The MedeA® software environment. ³⁹ is used for calculating and plotting the electronic band structure, as well as for the crystal structure visualization. The calculations reported in this work are performed using the Advanced Cyberinfrastructure Coordination Ecosystem: Services & Support (ACCESS) (formerly known as Extreme Science and Engineering Discovery Environment (XSEDE)) resources located at the Pittsburgh Supercomputing Center (PSC). ⁴⁰, the resources of the Center for Functional Nanomaterials (CFN) at Brookhaven National Laboratory (BNL), as well as the high-performance computing facilities located at the University of Northern Iowa (UNI).

II. b) Experimental methods

The NiFeMnAl bulk alloy was synthesized using arc-melting. The desired quantities of nickel, iron, manganese, and aluminum pieces were cut from corresponding commercially available (99.95% purity) metal pellets. The arc-melting was done in a constant flow of argon gas and the ingot was flipped and melted four times to insure homogeneity in the sample. The asprepared ingot was vacuum (~10⁻⁷ torr) annealed at various temperatures between 600 °C and 1000 °C but the annealed sample always showed tetragonal distortion. Therefore, we have included the data recorded only on the as-prepared sample in this report. The crystal structure of the sample was investigated using x-ray diffraction patterns recorded in a Rigaku Miniflex600 x-ray diffractometer and the magnetic measurements were performed using magnetometers on the Quantum Design VersaLab and Dynacool PPMS platforms.

III. Results

III. a) Computational results

Our calculations indicate that the lowest energy of NiFeMnAl corresponds to the regular cubic Heusler structure (space group F-43m), in agreement with the earlier report by Gao et al.²⁹ In this crystal structure, the atoms occupy the following Wyckoff positions: Ni(0,0,0), Fe(1/2,1/2,1/2), Mn(3/4,3/4,3/4), Al(1/4,1/4,1/4). Figure 1 shows the calculated density of states (DOS) (a) and band structure (b) of NiFeMnAl in the lowest-energy configuration, which corresponds to the lattice parameter of $a = 5.735 \,\text{Å}$. As one can see from Fig. 1. NiFeMnAl is half-metallic, and it is nearly spin-gapless semiconducting. In particular, as shown in Fig. 1 (b), what prevents this material from exhibiting a perfect SGS band structure, is a relatively small crossover of spin-up bands (red lines) with the Fermi level at the X symmetry point. The magnetic alignment of NiFeMnAl is ferromagnetic, with the calculated magnetization of 4.0 μ B / f.u., which is precisely what is expected from the Slater-Pauling rule. 12 The integer value of the magnetization is consistent with the half-metallic electronic structure. 41 The calculated element-resolved magnetic moments and the total magnetic moment per cell are summarized in Table 1. A small disagreement between the total magnetic moment and the sum of the individual atomic magnetic moments is due to the local charge and magnetization being calculated in atomic spheres that do not fill the volume of the unit cell exactly.¹⁸

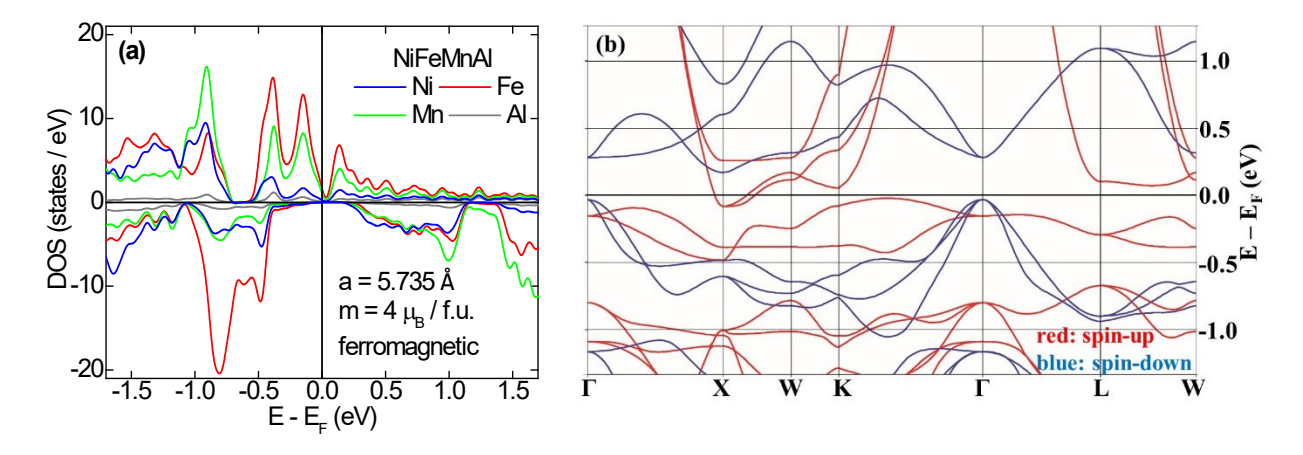


Figure 1. (a) Calculated element-resolved density of states of NiFeMnAl in the ground state. The element specific contributions are colored as indicated in the figure. Positive / negative DOS corresponds to majority / minority spin states, correspondingly. Vertical line indicates position of the Fermi level. (b) Calculated band structure of NiFeMnAl at equilibrium. Red and blue lines indicate spin-up and spin-down states, correspondingly. The horizontal line shows position of the Fermi level.

	Ni (μ _B /atom)	Fe (μ _B /atom)	Mn (μ _B /atom)	Al (μ_B /atom)	Total (µ _B /f.u.)
Magnetic moment (μ _B)	0.477	0.831	2.804	-0.091	4.000

Table 1. Calculated element resolved and total magnetic moments of NiFeMnAl at equilibrium.

Figure 2 (a) shows the calculated total energy (black line and squares) and total magnetic moment (blue line and circles) of NiFeMnAl under hydrostatic pressure, as a function of lattice constant (the calculated external pressure is shown in the inset). As one can see from the figure, the integer value of the total magnetic moment is retained over a significant range of lattice parameters under compression. At the same time, above the equilibrium lattice constant of a = 5.735 Å the total magnetic moment increases, first at a moderate rate, and then much steeper. This can serve as an indication of destroyed half-metallicity in NiFeMnAl under expansion (negative pressure). Figure 2 (b) shows calculated element-resolved magnetic moments of NiFeMnAl under hydrostatic pressure, as a function of lattice constant. In particular, it shows that the increase of the total magnetic moment at larger unit cell volumes results from an increase in the magnetic moment of Mn. At the same time, the magnetic moments of Fe and Ni decrease as the lattice constant is increased. A sharp increase of the Fe magnetic moment at the largest considered lattice parameter is probably a computational artifact, indicating the non-physical behavior of this system at that lattice constant.

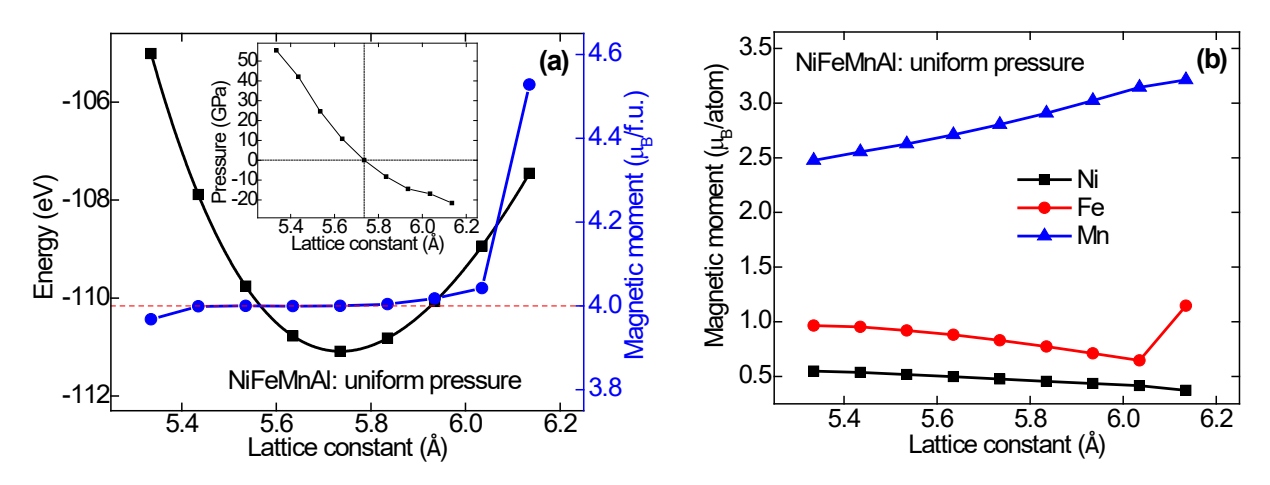


Figure 2. (a) Calculated total energy (black line and squares), total magnetic moment (blue line and circles), and external pressure (trace of a stress tensor, see inset) of NiFeMnAl under hydrostatic pressure, as a function of lattice constant. The (b) Calculated element resolved magnetic moments of NiFeMnAl under hydrostatic pressure, as a function of lattice constant. Blue line and triangles – Mn, black line and squares – Ni, red line and circles – Fe. Al is essentially non-magnetic and is not shown on this plot.

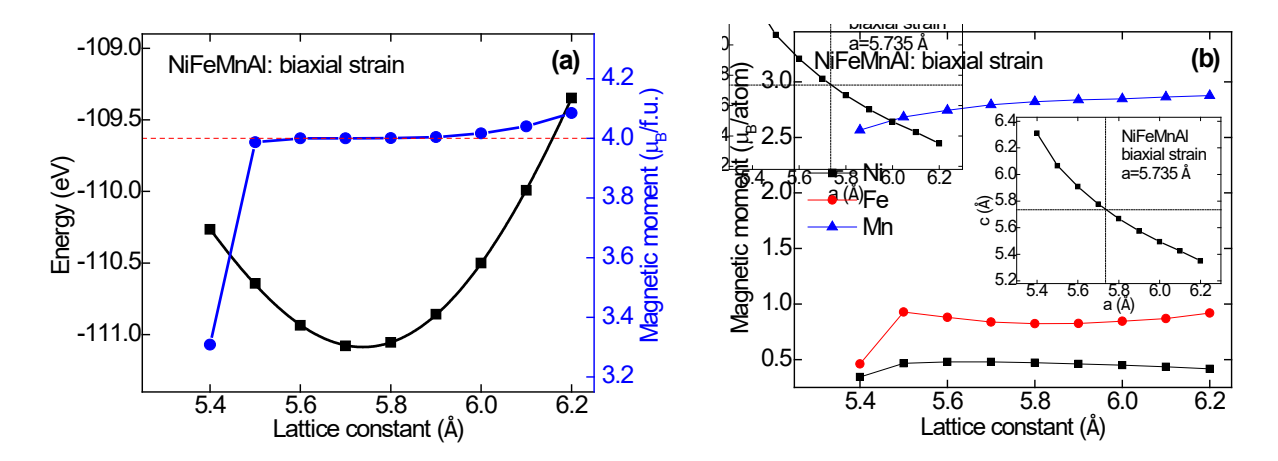


Figure 3. (a) Calculated total energy (black line and squares) and total magnetic moment (blue line and circles) of NiFeMnAl under biaxial strain, as a function of lattice constant. (b) Calculated element resolved magnetic moments of NiFeMnAl under biaxial strain, as a function of lattice constant. Blue line and triangles – Mn, black line and squares – Ni, red line and circles – Fe. Al is essentially non-magnetic and is not shown on this plot. The inset shows calculated out-of-plane lattice constant as a function of in-plane lattice constant (c vs. a) of NiFeMnAl under biaxial strain.

Figure 3 is a counterpart of figure 2, but calculated under biaxial strain, which is often a more realistic scenario in practical situations, such as in thin film heterostructures. Here, the biaxial strain is simulated by relaxing the out-of-plane lattice parameters (c) for each of the fixed in-plane lattice constant (a). The inset in Fig. 3 (b) shows calculated out-of-plane lattice constant as a function of in-plane lattice constant (c vs. a) of NiFeMnAl under biaxial strain. Qualitatively, figures 2 and 3 demonstrate similar behavior. At the same time, as shown in the Fig. 3 (a), the deviation of the total magnetic moment from its integer value at the larger in-plane lattice parameters happens in a somewhat more moderate way than in the case of hydrostatic pressure. This is likely due to a smaller change of the unit cell volume under biaxial strain compared with hydrostatic pressure, at given in-plane lattice parameters. Thus, one may expect that NiFeMnAl retains its half-metallic properties in a wider range of lattice parameter under biaxial strain than under hydrostatic pressure.

Figure 4 shows the calculated total density of states of NiFeMnAl under hydrostatic pressure (a) and biaxial strain (b). The in-plane lattice parameters as well as calculated spin-polarization values are shown in the figure. One interesting feature that can be seen in Fig. 4 (a) is that NiFeMnAl essentially undergoes a transition to the SGS state at the lattice constant of $a = 5.935 \,\text{Å}$. Here, the calculated spin polarization of around 6.6% has very little physical meaning,

since in the case of ideal SGS materials the formula we used to calculate spin polarizations $\left(P = \frac{N_{\uparrow}(\epsilon_F) - N_{\downarrow}(\epsilon_F)}{N_{\uparrow}(\epsilon_F) + N_{\downarrow}(\epsilon_F)}\right)$ results in $\frac{0}{0}$ indeterminacy. At the same time, as seen in Fig. 4 (b), the biaxial strain does not result in SGS transitions at larger lattice constants. Thus, if such a transition is desired, one should consider a potential scenario of uniform expansion of the unit cell volume, which can be achieved, at least in principle, by atomic substitution.³³

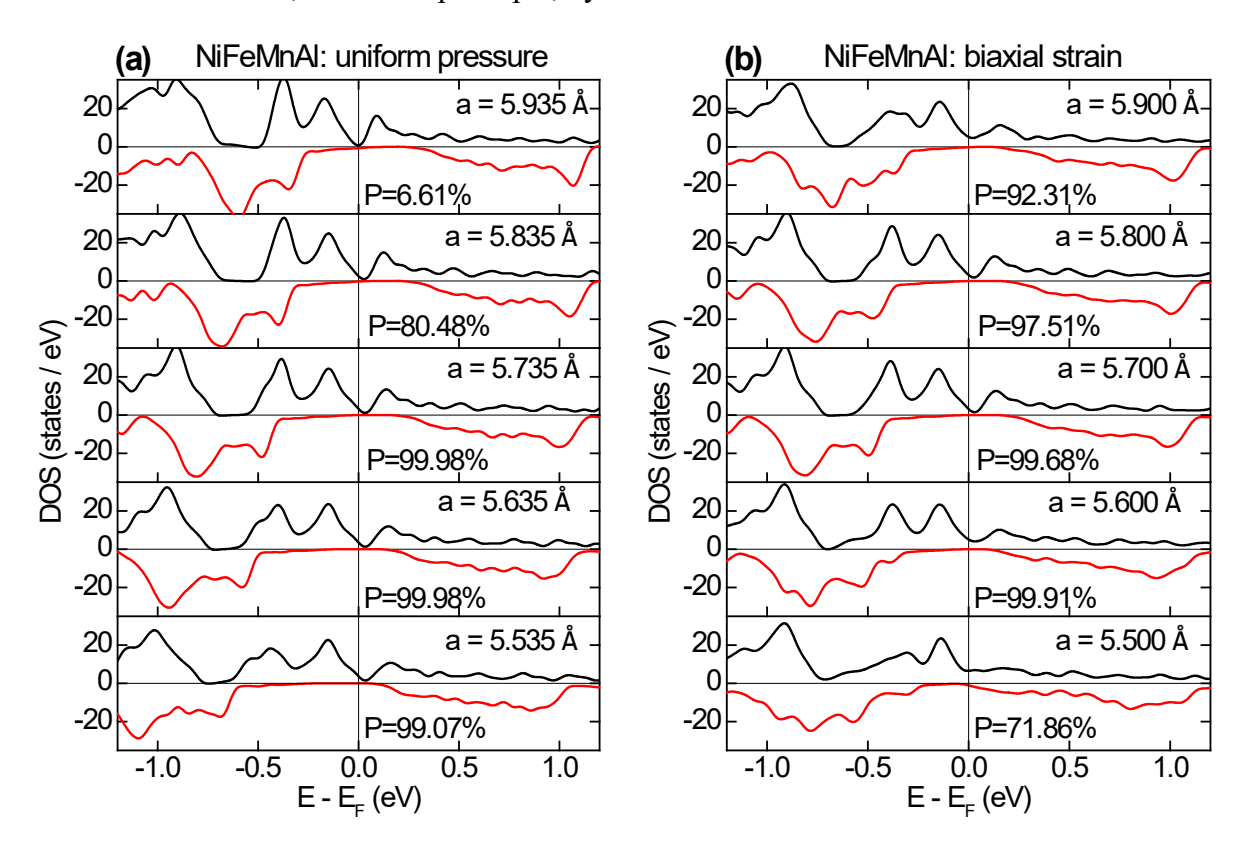


Figure 4. Calculated total DOS of NiFeMnAl under hydrostatic pressure (a) and biaxial strain (b). Positive DOS (black line) corresponds to majority-, negative DOS (red line) corresponds to minority-spin states. The in-plane lattice parameters as well as calculated spin-polarization values are shown in the figure. The vertical line corresponds to the Fermi level.

III. b) Experimental results

The room temperature x-ray diffraction (XRD) pattern of a powder sample prepared from the as-prepared NiFeMnAl ingot is shown in Fig. 5. The XRD pattern indicates that the as-prepared alloy has crystallized in the cubic structure with A2-type disorder, which is evident from the absence of (111) and (200) superlattice peaks. This may lead to a magnetic order different than the one predicted by theory as discussed above. In order to see if the crystalline order can be

improved with annealing, we annealed the sample at various temperatures between 600 °C and 1000 °C for 72 hours in a tubular vacuum furnace. However, all the annealed samples showed tetragonal distortion. For example, the XRD pattern of NiFeMnAl sample annealed at 650 °C for 72 hours is shown in the inset of Fig. 5 which contains an additional peak corresponding to the (112) plane of the tetragonal phase. T. Samanta et al. have also reported similar difficulty in the synthesis of NiFeMnGa and NiFeCuGa alloys. The lattice parameter of the as-prepared NiFeMnAl alloy determined from the x-ray diffraction pattern is a = 5.773 Å, which agrees well with the theoretical lattice parameter of 5.735 Å for the lowest-energy configuration.

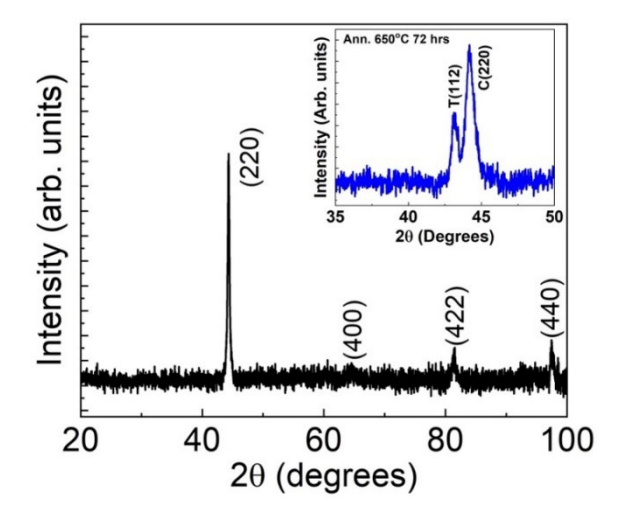


Fig. 5: Room temperature x-ray diffraction pattern of the as-prepared NiFeMnAl alloy. The inset shows the XRD pattern of the NiFeMnAl sample annealed at 650 °C for 72 hrs.

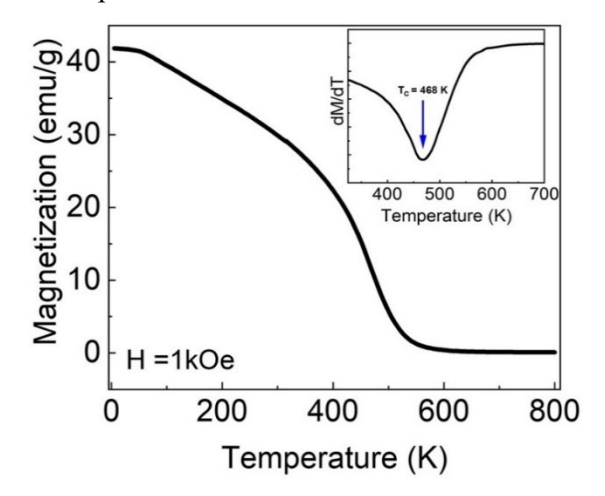


Fig.6: The thermomagnetic curve M(T) of the as-prepared NiFeMnAl alloy measured at 1 kOe external magnetic field. The inset shows the temperature derivative of the M(T) curve used to estimate the Curie temperature.

Figure 6 shows the temperature dependence of the magnetization M(T) of the as-prepared NiFeMnAl sample measured at an external magnetic field of 1 kOe. The magnetization of the sample remains almost stable as temperature increases from 5K to 50 K, and then starts to gradually decrease with the further increase in temperature reaching a Curie point at 468 K, where it undergoes a ferromagnetic to paramagnetic transition. This type of M(T) behavior is observed in other disordered Heusler alloys as well. ^{43,44}

Atomic swap	Fe-Al	Fe-Mn	Fe-Ni	Mn-Al	Ni-Al	Ni-Mn
$M (\mu_B / f.u.)$	5.275	4.001	3.698	4.053	4.433	3.001

Table 2. Calculated magnetization (M) values of NiFeMnAl for six possible forms of atomic swap disorder.

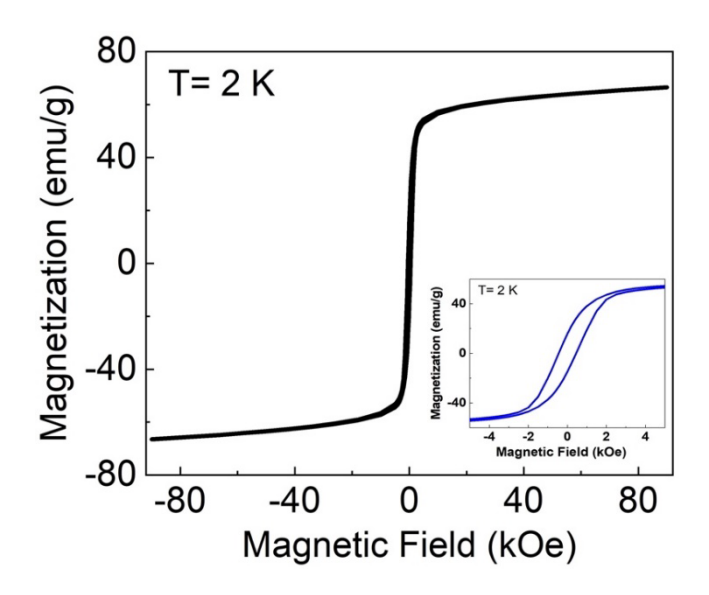


Fig. 7: The isothermal magnetization curve M(H) of the NiFeMnAl alloy measured at 2 K. The inset shows the expanded view of the M(H) curve near H=0 Oe.

The zero-field-cooled magnetic hysteresis curve M(H) recorded at 2 K is shown in Fig. 7. As shown in the inset of Fig. 7, where the M(H) loop is expanded near H=0, we can see a coercivity of about 0.5 kOe, which is unusually large for a cubic Heusler alloy. This is probably due to the aforementioned tetragonal distortion seen in the XRD patterns. The saturation magnetization M_S of the sample at 90 kOe field is about 67 emu/g (~2.3 μ_B/f . u.). This value of M_S is smaller than the one predicted by our first principles calculations (4 μ_B/f . u.). We attribute this discrepancy in the saturation magnetization to the observed disorder in the sample. The investigated sample

contains A2 type disorder, which may result in reduced magnetization. For example, we recently demonstrated that in another quaternary Heusler compound, MnCrVAl, A2-type disorder leads to reduced magnetization. ^{45,46} To confirm this conclusion, we also simulated atomic disorder in NiFeMnAl, by swapping a single atom of each element with an atom of another element. The results are summarized in Table 2. As one can see, only Ni-Mn atomic swap results in a significant decrease in the magnetization value. Since our samples exhibit A2 type disorder, where the Ni, Fe, Mn and Al atoms randomly occupy the available sites in the cubic lattice, any combinations of the situations considered in Table 2 may occur leading to a decrease in magnetization. Therefore, the calculated values of decreased magnetizations in some atomic exchanges are in qualitative agreement with the experimental observation.

IV. Conclusions

Here, we presented the results of a combined theoretical and experimental study of a quaternary Heusler compound NiFeMnAl. It is shown that this material exhibits a half-metallic electronic structure in the ground state and under a considerable range of external hydrostatic pressure and biaxial strain. The magnetic alignment of NiFeMnAl is ferromagnetic in the entire range of the considered pressure / strain. In addition, our calculations indicate that under hydrostatic pressure NiFeMnAl may undergo a spin-gapless semiconducting transition at the largest considered lattice constant. The practical feasibility of the considered alloy is confirmed by synthesizing this material. In particular, the bulk ingot of NiFeMnAl synthesized using arc melting crystallized in a cubic structure with A2 type disorder. The sample shows a high Curie temperature of about 468 K and a saturation magnetization of 2.3 μ_B/f . u. The saturation magnetization is smaller than that predicted for the half-metallic phase of this material, likely because of the disordered atomic arrangement. We hope that the presented results may be useful for researchers working on practical applications of spin-based electronics.

Acknowledgments

This research is supported by the *National Science Foundation* (NSF) under Grant Numbers 2003828 and 2003856 via DMR and EPSCoR. This work used the Advanced

Cyberinfrastructure Coordination Ecosystem: Services & Support (ACCESS) (formerly known as Extreme Science and Engineering Discovery Environment (XSEDE)), which is supported by National Science Foundation grant number ACI-1548562. This work used the XSEDE Regular Memory (Bridges 2) and Storage (Bridges Ocean) at the Pittsburgh Supercomputing Center (PSC) through allocation TG-DMR180059, and the resources of the Center for Functional Nanomaterials, which is a U.S. DOE Office of Science Facility, and the Scientific Data and Computing Center, a component of the Computational Science Initiative, at Brookhaven National Laboratory (BNL) under Contract No. DE-SC0012704.

References

R. de Groot, F. Mueller, P. van Engen, and K. Buschow, Phys. Rev. Lett. **50**, 2024 (1983).

² J. P. Velev, P. A. Dowben, E. Y. Tsymbal, S. J. Jenkins, and A. N. Caruso, Surf. Sci. Rep. **63**, 400 (2008).

³ I. Galanakis, J. Phys. Condens. Matter **14**, 6329 (2002).

⁴ I. Galanakis, J. Magn. Magn. Mater. **288**, 411 (2005).

⁵ M. Ležaic, I. Galanakis, G. Bihlmayer, S. Blügel, J. Phys. Condens. Matter 17, 3121 (2005).

⁶ I. Galanakis, M. Ležaic, G. Bihlmayer, S. Blügel, Phys. Rev. B **71**, 214431 (2005).

⁷ I. Galanakis, K. Özdoğan, E. Şaşıoğlu, J. Appl. Phys. **104**, 083916 (2008).

⁸ S. Jenkins, D. King, Surf. Sci. **494**, L793 (2001).

⁹ S. Jenkins, D. King, Surf. Sci. **501**, L185 (2002).

¹⁰ G. Wijs, R. de Groot, Phys. Rev. B **64**, R020402 (2001).

¹¹ A. Debernardi, M. Peressi, A. Baldereschi, Mater. Sci. Eng. C-Bio. S 23, 743 (2003).

¹² I. Galanakis, P. Dederichs, N. Papanikolaou, Phys. Rev. B **66**, 174429 (2002).

¹³ E. Şaşıoğlu, L. Sandratskii, and P. Bruno, Phys. Rev. B **72**, 184415, (2005).

¹⁴ B. Balke, G. H. Fecher, J. Winterlik, and C. Felser, Appl. Phys. Lett. **90**, 152504 (2007).

¹⁵ H. Kurt, K. Rode, M. Venkatesan, P. Stamenov, and J. M. D. Coey, Phys. Status Solidi B **248**, 2338 (2011).

J. Winterlik, S. Chadov, A. Gupta, V. Alijani, T. Gasi, K. Filsinger, B. Balke, G. H. Fecher, C. A. Jenkins, F. Casper, J. Kübler, G. Liu, L. Gao, S. Parkin, and C. Felser, Adv. Mater. 24, 6283 (2012).

¹⁷ I. Galanakis, in *Heusler Alloys*, Springer Series in Materials Science 222, C. Felser and A. Hirohata (eds.), Springer International Publishing Switzerland 2016.

P. Lukashev, P. Kharel, S. Gilbert, B. Staten, N. Hurley, R. Fuglsby, Y. Huh, S. Valloppilly, W. Zhang, K. Yang, R. Skomski, and D. J. Sellmyer, Appl. Phys. Lett. 108, 141901 (2016).

J. Ma, J. He, D. Mazumdar, K. Munira, S. Keshavarz, T. Lovorn, C. Wolverton, A. Ghosh, and W. Butler, Phys. Rev. B 98, 094410 (2018).

²⁰ A. Dehghan, S. Davatolhagh, J. Alloys Compd. 772, 132 (2019).

²¹ K. Hanssen, P. Mijnarends, Phys. Rev. B **34**, 5009 (1986).

²² K. Hanssen, P. Mijnarends, L. Rabou, K. Buschow, Phys. Rev. B **42**, 1533 (1990).

W. van Roy, M. Wojcik, E. Jdryka, S. Nadolski, D. Jalabert, B. Brijs, G. Borghs, J. De Boeck, Appl. Phys. Lett. 83, 4214 (2003).

²⁴ S. Chaudhuri, D. Salas, V. Srihari, E. Welter, I. Karaman, P. Bhobe, Sci Rep 11, 524 (2021).

- ²⁵ T. Krenke, E. Duman, M. Acet, E. Wassermann, X. Moya, L. Mañosa, and A. Planes, Nat. Mater 4, 450 (2005).
- ²⁶ I. Takeuchi, O. Famodu, J. Read, M. Aronova, K. Chang, C. Craciunescu, S. Lofland, M. Wuttig, F. C. Wellstood, L. Knauss, and A. Orozco, Nat. Mater 2, 180 (2003).
- W. Shi, L. Muechler, K. Manna, Y. Zhang, K. Koepernik, R. Car, J. van den Brink, C. Felser, and Y. Sun, Phys. Rev. B **97**, 060406(R) (2018).
- ²⁸ C. Shekhar, A. Nayak, Y. Sun, M. Schmidt, M. Nicklas, I. Leermakers, U. Zeitler, Y. Skourski, J. Wosnitza, Z. Liu, Y. Chen, W. Schnelle, H. Borrmann, Y. Grin, C. Felser, and B. Yan, Nat. Phys 11, 645 (2015).
- ²⁹ Q. Gao, I. Opahle, and H. Zhang, Phys. Rev. Materials **3**, 024410 (2019).
- ³⁰ X. L. Wang, Phys. Rev. Lett. **100**, 156404 (2008).
- P. Kharel, W. Zhang, R. Skomski, S. Valloppilly, Y. Huh, R. Fuglsby, S. Gilbert, and D. J. Sellmyer, J. Phys. D: Appl. Phys. 48, 245002(2015).
- ³² S. Ouardi, G. H. Fecher, and C. Felser, Phys. Rev. Lett. **110**, 100401 (2013).
- ³³ E. O'Leary, A. Ramker, D. VanBrogen, B. Dahal, E. Montgomery, S. Poddar, P. Kharel, A. Stollenwerk, and P. Lukashev, J. Appl. Phys., **128**, 113906 (2020).
- ³⁴ L. Stuelke, L. Margaryan, P. Kharel, P. Shand, P. Lukashev, J. Magn. Magn. Mater 553, 169267 (2022).
- ³⁵ G. Kresse and D. Joubert, Phys. Rev. B **59**, 1758 (1999).
- ³⁶ P. Blöchl, Phys. Rev. B **50**, 17953 (1994).
- ³⁷ J. Perdew, K. Burke, and M. Ernzerhof, Phys. Rev. Lett. **77**, 3865 (1996).
- ³⁸ M. Methfessel and A. T. Paxton, Phys. Rev. B **40**, 3616 (1989).
- ³⁹ MedeA-2.22, Materials Design, Inc., San Diego, CA, USA, 2017.
- J. Towns, T. Cockerill, M. Dahan, I. Foster, K. Gaither, A. Grimshaw, V. Hazlewood, S. Lathrop, D. Lifka, G. D. Peterson, R. Roskies, J. R. Scott, N. Wilkins-Diehr, "XSEDE: Accelerating Scientific Discovery", Computing in Science & Engineering, vol.16, no. 5, pp. 62-74, Sept.-Oct. 2014.
- ⁴¹ I. Tutic, J. Herran, B. Staten, P. Gray, T. Paudel, A. Sokolov, E. Tsymbal, and P. Lukashev, J. Phys.: Condens. Matter **29**, 075801 (2017).
- ⁴² T. Samanta, S. Chaudhuri, S. Singh, V. Srihari, A. Nigam, and P. Bhobe, J. Alloys Compd. **819**, 153029 (2020).
- ⁴³ A. Nelson, P. Kharel, Y. Huh, R. Fuglsby, J. Guenther, W. Zhang, B. Staten, P. Lukashev, S. Valloppilly, and D. Sellmyer, J. Appl. Phys. **117**, 153906 (2015).
- P. Kharel, W. Zhang, R. Skomski, S. Valloppilly, Y. Huh, R. Fuglsby, S. Gilbert, and D. Sellmyer, J. Phys. D: Appl. Phys. 48, 245002 (2015).
- P. Kharel, J. Herran, P. Lukashev, Y. Jin, J. Waybright, S. Gilbert, B. Staten, P. Gray, S. Valloppilly, Y. Huh, and D. Sellmyer, AIP Adv. 7, 056402 (2017).
- ⁴⁶ J. Herran, R. Dalal, P. Gray, P. Kharel, and P. Lukashev, J. Appl. Phys. **122**, 153904 (2017).